Numerical investigations of the dynamic response of a floating bridge under environmental loadings

Yanyan Sha[a,b]* , Jørgen Amdahl[a,b], Aleksander Aalberg[a] and Zhaolong Yu[a,b]

[a] *Department of Marine Technology, Norwegian University of Science and Technology, Trondheim, Norway*

[b] *Centre for Autonomous Marine Operations and Systems, Norwegian University of Science and Technology, Trondheim, Norway*

*corresponding author: Yanyan Sha, Tel.: +47-73595685. E-mail: yanyan.sha@ntnu.no

Numerical investigations of the dynamic response of a floating bridge under environmental loadings

Floating bridges across wide and deep fjords are subjected to the environmental wind and wave loadings. The dynamic response of the bridges under such loadings is an important aspect, which should be carefully investigated in the design process. In this study, a floating bridge concept, which consists of two cable-stayed spans and nineteen continuous spans, is selected. A finite element model of the bridge is established using the software USFOS. An eigenvalue analysis is first conducted to obtain the natural periods and vibration modes of the bridge. It is found that the period of the first mode is typically in the order of one minute or more. This implies that the amplified response effect should also be evaluated for the second-order wave load in addition to the first-order wave load. By performing a nonlinear time domain dynamic analysis, the bridge dynamic responses from wind and wave loadings are obtained. The effects of the wind load, first-order and second-order wave loads are studied considering different load combinations. Structural responses including girder displacements, accelerations and moments are investigated for each load combination.

Keywords: floating bridge; environmental loads; time-domain analysis.

1. Introduction

The Norwegian Public Roads Administration is running a project 'Coastal Highway Route E39' which aims to replace the existing ferries by bridges or tunnels along the west coast of Norway. These installations will be constructed to cross the large and deep fjords, which may have a length and depth up to 5000 m and 600 m, respectively. This critical site condition makes it almost impossible to build bridges with fixed foundations. Therefore, floating bridges become a better choice as the conventional piers or pile foundations are not required. The superstructure of the floating bridge is alternatively supported by floating pontoons or floaters. Many very large floating structures (VLFS) have been designed and constructed in the past several decades. They are primarily used as floating airports, ports and storage facilities. The experience from

these VLFS can deliver useful information for floating bridges. However, the design and construction experience is still quite limited for large-scale floating bridges. Hence, further research is required to extend the knowledge from the fixed-foundation bridges to the bridges with floating foundations.

The hydrodynamic response of floating structures including ships, offshore platforms and wind turbines under wave loadings has been extensively studied by Chakrabarti (1987), Faltinsen (1993) and Kvittem et al. (2012). Both frequency-domain and time-domain analyses can be carried out to investigate the structural response under wave loadings. Compared with time-domain analyses, frequency-domain analyses are simpler and faster. However, for transient responses and for nonlinear motions, frequency-domain analyses are more complicated as they require the evaluation of several nonlinear eigenmodes and the integration over a wide range of frequencies. Therefore, it is necessary to perform a time-domain analysis (Salvatori and Borri 2007, Watanabe et al. 2004).

Apart from wave loads, wind loads are also prominent for bridges, especially for bridges with long spans (Boonyapinyo et al. 1994). Hence, the analysis of the wind-induced response for long-span bridges is deemed to be necessary. Time-domain dynamic analyses of wind-sensitive structures including long-span bridges have been extensively conducted (Aas-Jakobsen and Strømmen 1998, Santos et al. 1993). The nonlinear response of the bridges can be calculated with sufficient accuracy by means of a time-domain analysis (Cao et al. 2000). For the floating bridge concepts, it is more important to carefully investigate the wind effect as they are generally more compliant than bridges with fixed foundations.

In this paper, a bridge concept proposed for Bjornefjorden is selected as an example and the numerical model of the bridge is established in the finite element (FE)

software USFOS (Søreide et al. 1993). The first-order and second-order wave loads and the wind load are calculated numerically and applied to the FE bridge model as external forces without dependence on the structural displacement. The bridge response to wave and wind loadings is obtained through time-domain simulations. The effects of the wind load and the first-order and second-order wave loads are studied considering different load combinations.

2. Numerical modelling

The floating bridge concept in this study contains two cable-stayed spans and nineteen floating continuous spans as shown in Figure 1. In the southern part, two cable-stayed spans are connected to a fixed reinforced concrete tower with 84 cables. The remaining continuous spans are supported by the floating pontoons. The distance between every two pontoons is 197 m in the continuous part. The bridge has a curved shape in the horizontal plane with a radius of 5000 m. The purpose of the curved design is to increase the transverse stiffness by means of the arch action. The girders in the cable-stayed span have a height of 55 m above the sea level, and this span is designed as a navigation channel for the passing ships. The bridge girder height decreases gradually from the south side to the north side. The bridge girders to the north of the sixth pontoon have a low clearance of 11.75 m from the sea surface. The particulars of the floating bridge are listed in Table 1.
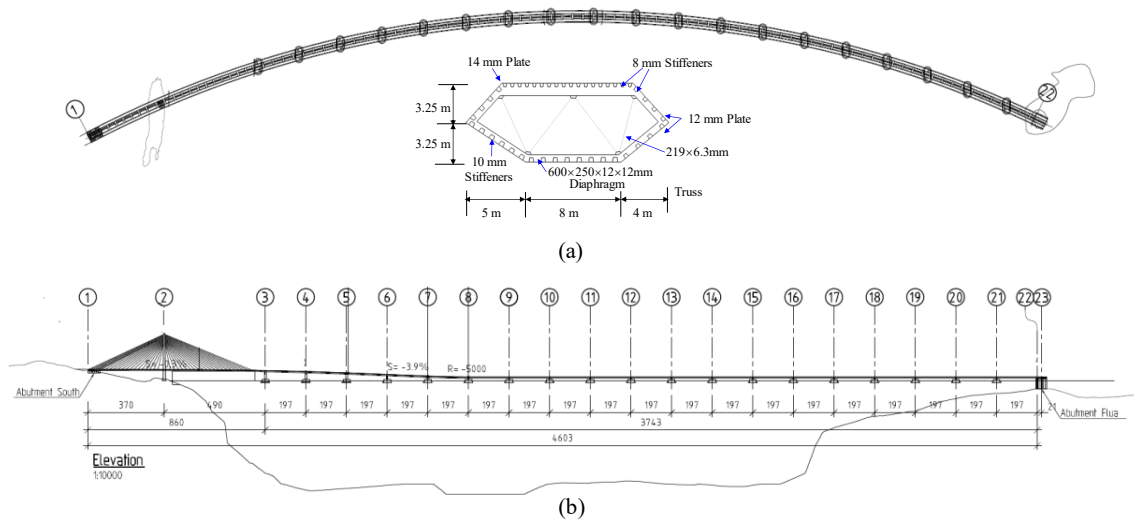
Figure 1. Floating bridge concept for Bjornefjorden, (a) top view, (b) side view.

Table 1. Particulars of the floating bridge.

Parameter	Value (m)
Bridge length	4500
Tower height	215.6
Girder width: cable-stayed span/continuous span	15/17
Girder height: cable-stayed span/continuous span	5/6.5
Crossbeam width	8
Crossbeam height: cable-stayed span/continuous span	5/6.5
Column diameter	8
Pontoon dimension	$78 \times 38 \times 14$

2.1 Structural modelling

Detailed modelling is applied to all bridge components including the twin girders, crossbeams, columns, pontoons, cables and the bridge tower (Sha and Amdahl 2017).

The Vierendeel bridge girders consist of two parallel steel boxes spaced sufficiently apart in order to give adequate bending stiffness and buckling capacity. The girder heights in the cable-stayed spans and continuous spans are 5 m and 6.5 m, respectively. The sectional property of the bridge girder varies along the length of the bridge. Generally, the plate thickness and stiffener dimension increase from the span section to the support section. The parallel steel boxes are connected by rectangular crossbeams with approximately 40 m spacing in the cable-stayed spans and 50 m

spacing in the continuous spans. The steel material used in the bridge girders and crossbeams has a characteristic yield stress of 460 MPa.

The stay cables support the bridge girder every 20 m in the south. The stay cables are constructed of high strength steel strands (S1860). According to Eurocode (Institution 2004), the stay cables can be utilized to 56% of the tensile strength of the steel cables due to permanent loads only. For a traditional cable-stayed bridge, the stay cables are usually utilized to 40 % of the breaking strength due to the permanent loads only. As the safety factor for the permanent loads has increased from 1.2 to 1.35 and in addition the stay cables in a floating bridge are subjected to the wave loads, the utilization ratio for the permanent loads should be decreased (COWI 2016). Therefore, the stay cables are dimensioned by using a utilization ratio of 28 % due to the permanent loads in the initial design. The cross-sectional area of the cable is calculated based on this utilization ratio for the permanent loads. It varies from 0.00705 m^2 to 0.0138 m^2 as the cable length increases. In the analysis, the stay cables are first pre-tensioned to balance the bending moments in the girder due to permanent loads.

The stay cables are connected to a reinforced concrete tower which has a rectangular cross-sectional shape. The dimension of the tower cross section reduces from 20×12 m at the base to 12×7 m at the top. The tower is modelled with high strength to ensure a minor deformation in the tower.

In the continuous spans, the floating bridge is supported by 19 equal pontoons made of lightweight concrete. The total height of each pontoon is 14 m with a 10 m draft. The pontoon has a 5 m wide flange at the bottom with the purpose of increasing the added mass for the heave motion. The pontoons are connected to the bridge girders by two columns at each axis. The two columns are aligned perpendicular to the curved bridge girder axis. All columns are made of S460 steel and have a diameter of 8 m.

The numerical model of the whole bridge is developed with beam elements in USFOS as shown in Figure 2 (a). The beam element is based on the nonlinear Green strain formulation and an updated Lagrange (incremental-iterative) procedure allowing for large displacements and moderate elastic, axial strains. The influence of axial force on the bending stiffness of the element is introduced through the so-called Livesley's stability functions (Livesley 2013).

The element formulation is based on linearly elastic behaviour up to first yield while nonlinear material behaviour is modelled with plastic hinges. In the present analysis, the bridge girder is assumed to be elastic. It is likely that collapse will be triggered by first occurrence of local failure of stiffened panels. Local failure has not been checked in the present study, as focus has been placed on getting a better understanding of the contributions from the first and the second order wave loads and the wind loads to the global response. The main advantage of the program is that a physical structural element can be modelled by only one finite beam element. This modelling technique is computationally efficient and makes it possible to analyse large complex structures. For example, each bridge column, stay cable and crossbeam are modelled by only one beam element. The bridge girders between every two pontoons are modelled by nine beam elements due to the variation of girder's sectional properties. For the whole floating bridge, only 911 beam elements are used to establish the numerical model.
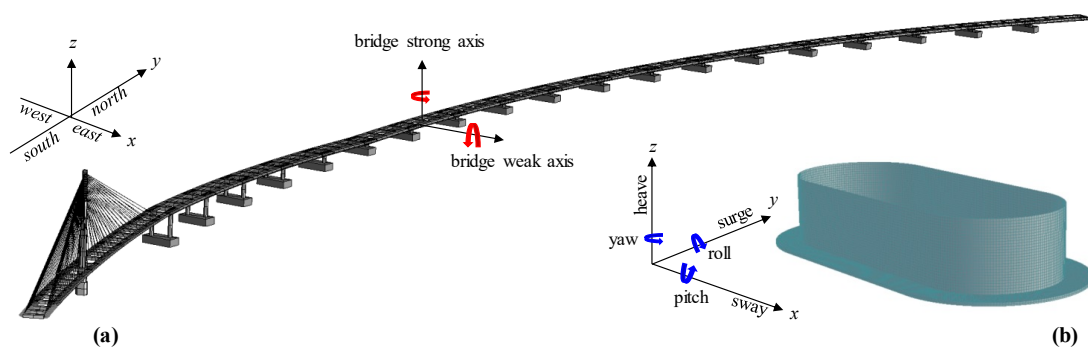
Figure 2. Numerical models, (a) global bridge model, (b) pontoon model.

Both ends of the bridge are fixed in all translational and rotational degrees of freedom. The bottom of the bridge tower is also fixed in all degrees of freedom since it will be constructed with a fixed foundation on the southern bank.

To analyze the dynamic behaviour of the bridge under environmental loads, it is necessary to consider the wave loads on the pontoons and the wind load on the bridge tower, cables, columns and girders. The equation of motion of the bridge under such loads can be written as

$$\left[M\right]\{\ddot{u}\}+\left[C\right]\{\dot{u}\}+\mathrm{r}\{u\}=\{F(t)\}, \tag{1}$$

where $\left[M\right]$ and $\left[C\right]$ represent the structural mass and damping matrix, respectively. $\{u\}$ is the vector of displacement. $\mathrm{r}\{u\}$ is the internal force vector on the displacements and $\{F(t)\}$ is the vector of external forces applied to the bridge structure.

In the USFOS program, the Hilber-Hughes-Taylor integration scheme (Hilber et al. 1977) is adopted to solve the second-order differential equations as expressed by Equation 1. This method is a one-parameter, multi-step implicit method which applies time averaging of the damping, stiffness and load terms by the α-parameter (Jia 2014).

2.2 Hydrodynamic modelling

The major difference between a floating bridge and a fixed foundation bridge is that the pontoons are exposed to wave loads. A critical aspect in developing the numerical model of the floating bridge is thus the hydrodynamic modelling of the pontoons.

To calculate the hydrodynamic properties of the pontoons, a structural model of the pontoon is developed as shown in Figure 2 (b). The added mass and potential

damping at discrete frequencies are obtained by linear potential theory using the software WADAM (Veritas 1994). As the direct integration method can be sensitive to the sharp edge of the bottom flange (Faltinsen 1993), the far field integration method is utilized to calculate the second-order transfer functions, and a mesh size of 0.5 m is selected for the model after running a mesh convergence study. This mesh size is also used for all the other hydrodynamic calculations.

Numerical results for the selected components of the added mass and potential damping are displayed in Figure 3. For sway and surge, the added mass curves appear to approach asymptotic values for large periods. Hence, the added mass values of 4.59 Mkg and 17.4 Mkg at a very large period are used for these two components respectively. For the heave motion, an added mass of 35.6 Mkg is selected at a period of 11 s. This period is in the same range of the eigenmodes which are dominated by vertical motions. The value of the potential damping is set to zero for sway and surge and 1.65 Mkg/s for heave according to Figure 3.
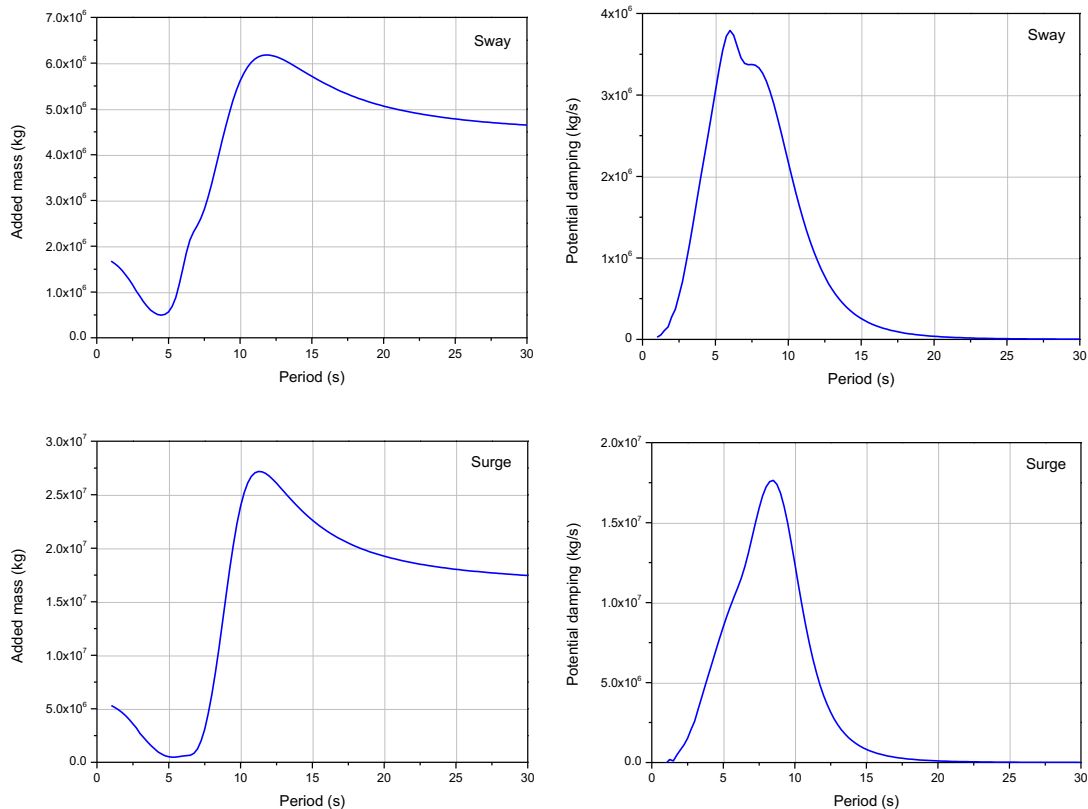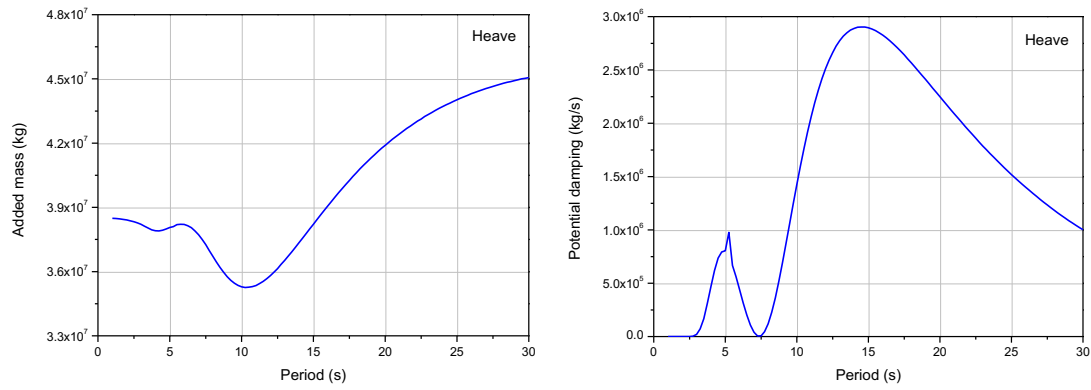
Figure 3. Added mass and potential damping curves of the pontoon.

2.3 Eigenvalue analysis

An eigenvalue analysis is first conducted to explore the dynamic characteristics of the floating bridge. In total, 50 eigenmodes were calculated. The periods and vibration characteristics of 20 selected modes are listed in Table 2. The first two modes are dominated by the in-plane horizontal bending. The third to ninth mode have significant contributions from the rotation about the bridge longitudinal axis. Vertical vibrations from the pontoon heave motion dominate the modes 10-15. The first 15 modes are expected to be most important for the wind and second-order wave loads while modes 34 to 38 are in the region of the first-order wave load with a period of 6 s. Three typical mode shapes representing horizontal bending, rotation about the y-axis, and vertical motion are illustrated in Figure 4.

Table 2. Bridge natural periods and dominating motions.

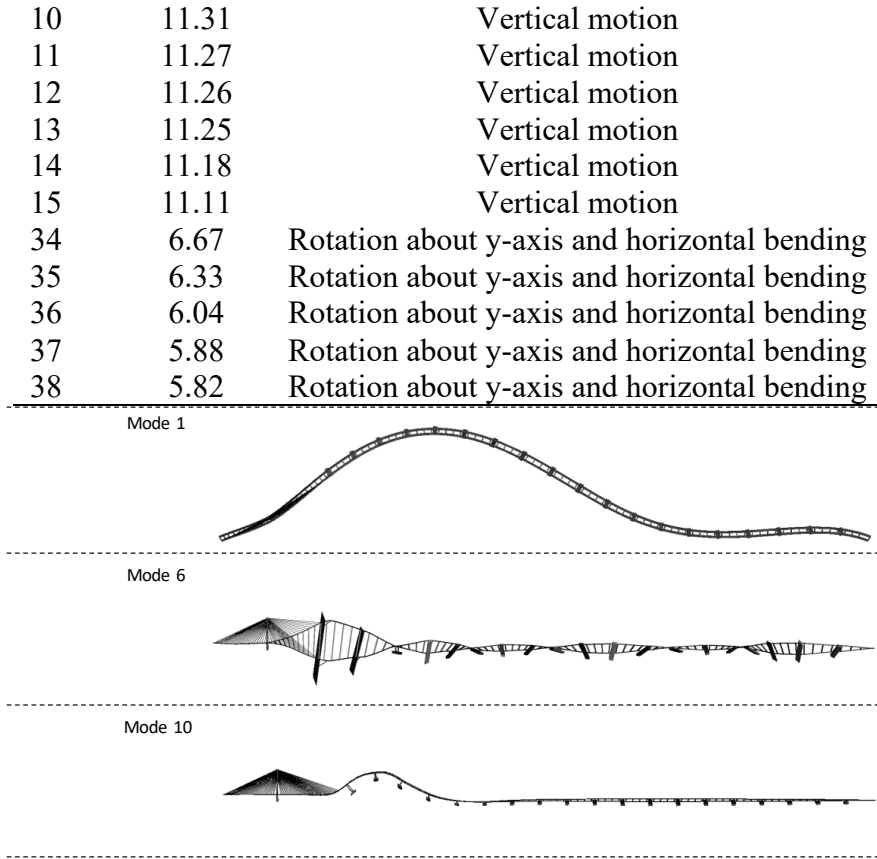| Mode	Period (s)	Dominating motion
1	65.07	Horizontal bending
2	37.02	Horizontal bending
3	22.65	Horizontal bending and rotation about y-axis
4	20.87	Horizontal bending and rotation about y-axis
5	15.65	Horizontal bending and rotation about y-axis
6	13.52	Rotation about y-axis
7	13.13	Rotation about y-axis
8	11.59	Horizontal bending and rotation about y-axis
9	11.38	Horizontal bending and rotation about y-axis

10	11.31	Vertical motion
11	11.27	Vertical motion
12	11.26	Vertical motion
13	11.25	Vertical motion
14	11.18	Vertical motion
15	11.11	Vertical motion
34	6.67	Rotation about y-axis and horizontal bending
35	6.33	Rotation about y-axis and horizontal bending
36	6.04	Rotation about y-axis and horizontal bending
37	5.88	Rotation about y-axis and horizontal bending
38	5.82	Rotation about y-axis and horizontal bending

Figure 4. Selected mode shapes.

3. Wave loads

3.1 First-order waves

The time histories for the first-order (linear) wave forces are calculated using the transfer functions calculated in WADAM. The obtained wave force components are then summed over all wave frequencies according to Equation 2. The effect of the curved shape of the pontoon and the contribution from the bottom flange are accounted for in the numerical model as shown in Figure 2 (b). The total excitation wave force time history $F_{exi,t}(t)$ and the wave elevation $\zeta(t)$ are given by Equation 2 and 3.

$$F_{exc,i}(t) = \sum_{j=1}^{N} \zeta_{a,j} \cdot \left| H_i(\omega_j) \right| \cdot \cos(\omega_j \cdot t + \delta_j(\omega_j) + \varepsilon_j), \qquad (2)$$

$$\zeta(t) = \sum_{j=1}^{N} \zeta_{a,j} \cdot \cos(\omega_j \cdot t + \varepsilon_j),$$ (3)

where $\zeta_{a,j}$ and $H_i(\omega_j)$ are the wave amplitude and the transfer function, respectively. ω_j is the wave frequency component, t is the time instant and ε is a random phase angle. $\delta_j(\omega_i)$ accounts for the phase angle between the force and the wave elevation. The subscript i and j designate the degree of freedom and frequency component numbers, respectively. Both equations assume that irregular waves can be expressed by a superposition of all regular wave components in a sea state based on linear wave theory (Faltinsen 1993).

Provided that the transfer functions and the phase angles in Equation 2 are established, the only unknown parameter is the wave amplitude ζ_a. It can be calculated from a wave spectrum $S(\omega)$ by means of Equation 4, where $\Delta\omega$ is the frequency increment.

$$\zeta_a = \sqrt{2 \cdot S(\omega_j) \cdot \Delta\omega}.$$ (4)

As the site wave data is still under measurement (COWI 2016), the Joint North Sea Wave Project (JONSWAP) Spectrum is used in this study (Hasselmann et al. 1973). It can be expressed by the formulation as shown in Equation 5,

$$S(\omega) = \left(1 - 0.287\ln(\gamma) \cdot \frac{5}{16} H_s^2 \omega_p^4 \cdot \omega^{-5} \cdot \exp\left[-\frac{5}{4}\left(\frac{\omega}{\omega_p}\right)^{-4}\right] \cdot \gamma^{\exp\left[-0.5\left(\frac{\omega - \omega_p}{\sigma \cdot \omega_p}\right)^2\right]}\right),$$ (5)

where γ is a parameter defining the shape of the spectrum peak, H_s is the significant wave height, ω_p is the peak frequency, σ describes the width of the peak

and $S(\omega)$ is the spectrum value for wave frequency ω. The spectrum for $H_s = 3$ m and

$T_p = 6$ s which is used in this study is shown in Figure 5.
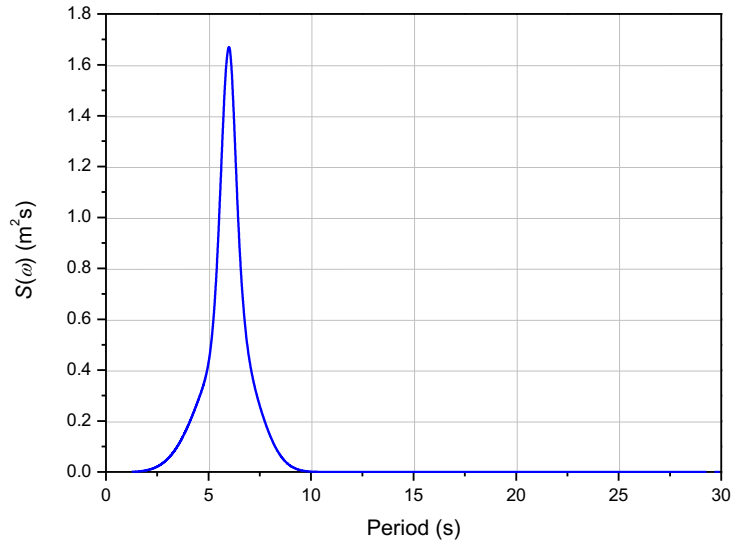

Figure 5. JONSWAP spectrum used for the wind generated sea.

3.2 Second-order waves

Linear wave theory only accounts for the loads which have the same frequency as the incident waves. A floating structure will in general also exposed to nonlinear wave forces. These include the mean drift forces with so-called sum and difference frequencies (Faltinsen 1993). Difference frequency forces are caused by the presence of different frequency components in an irregular sea state. They are varying slowly and may be critical for floating structures with natural periods in the range of 1-2 minutes. The floating bridge has a first natural period of around 1 minute which may be resonant with the difference frequency forces.

To obtain the slow-drift force, a similar formulation as the linear excitation force is introduced, given by Equation 6 (Faltinsen 1993):

$$F_i^{sv} = \sum_{j=1}^{N}\sum_{k=1}^{N} \zeta_{a,j} \cdot \zeta_{a,k} \left\{ T_{jk}^{ic} \cos\left[(\omega_k - \omega_j)t + (\varepsilon_k - \varepsilon_j)\right] + T_{jk}^{is} \sin\left[(\omega_k - \omega_j)t + (\varepsilon_k - \varepsilon_j)\right] \right\}, \quad (6)$$

where F_i^{sv} is the slow-drift wave load. ζ_a is the wave amplitude and t is the time instant. ω is the wave frequency and ε is the random phase angle. T_{jk}^{ic} and T_{jk}^{is} are the second-order transfer functions. Further, the subscripts j and k refer to the wave component number. N is the total amount of components.

By using Newman's approximation (Newman 1974), it is possible to express the off-diagonal terms of the second-order transfer functions by the diagonal ones as shown by Equation 7 and 8. The benefit of this approach is that the diagonal terms correspond to the mean drift coefficients. Hence, it can be calculated using only the linear velocity potential which is easier and faster to solve.

$$T_{jk}^{ic} = T_{kj}^{ic} = 0.5\left(T_{jj}^{ic} + T_{kk}^{ic}\right) \tag{7}$$

$$T_{jk}^{is} = T_{kj}^{is} = 0 \tag{8}$$

By substituting Equation 7 and 8 into Equation 6, it can be simplified into a single summation as presented in Equation 9, where only the diagonal terms of the cosine transfer functions are required:

$$F_i^{sv}(t) = 2\left[\sum_{j=1}^{N} \zeta_{a,j} \cdot T_{jj}^{ic}(\omega_j)^{1/2} \cos(\omega_j \cdot t + \varepsilon_j)\right]^2 . \tag{9}$$

Similar to the linear wave force, the time histories for the slowly varying drift forces are established using mean drift coefficients from the WADAM analysis together with Newman's approximation.

3.3 3.3. Simulated wave loads

In the analysis, both the first-order and second-order wave loads are considered. The generated wave loads are introduced as individual time histories applied to each of the

19 pontoons. Examples of the first-order and second-order wave force time histories in the global x-direction are illustrated in Figure 6. It is observed that the amplitude of the second-order wave force is significantly smaller than the first-order wave force and the period is much longer. The difference can also be observed in the spectrum density graph as shown in Figure 7. The first-order wave force dominates the frequency range from 0.1 to 0.25 Hz, which coincides with some of the higher modes of the bridge. The second-order wave force concentrates in the range of very low frequencies up to 0.03 Hz. This frequency range is important as the first and second horizontal bending modes of the bridge are in the same range. All the first-order and second-order wave forces are then applied as nodal loads in the centre of the waterplane area at the free surface of each pontoon. In the analysis, long-crested waves are assumed.
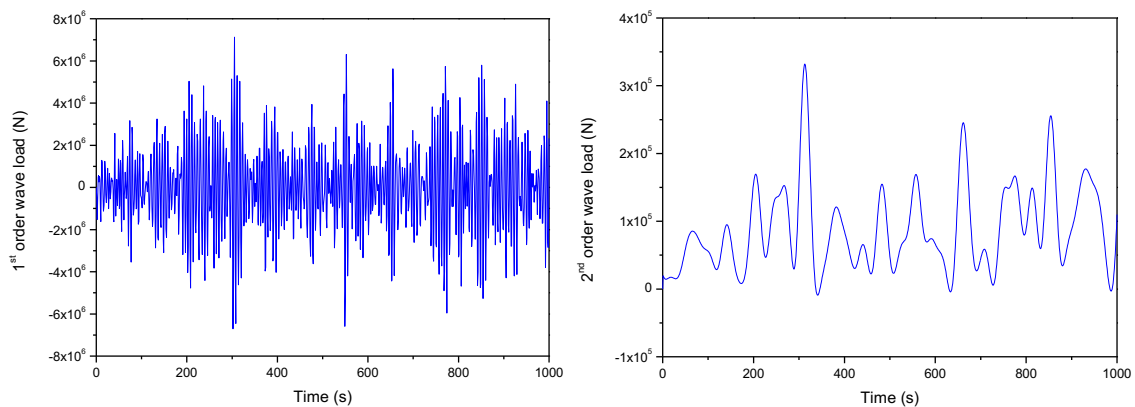

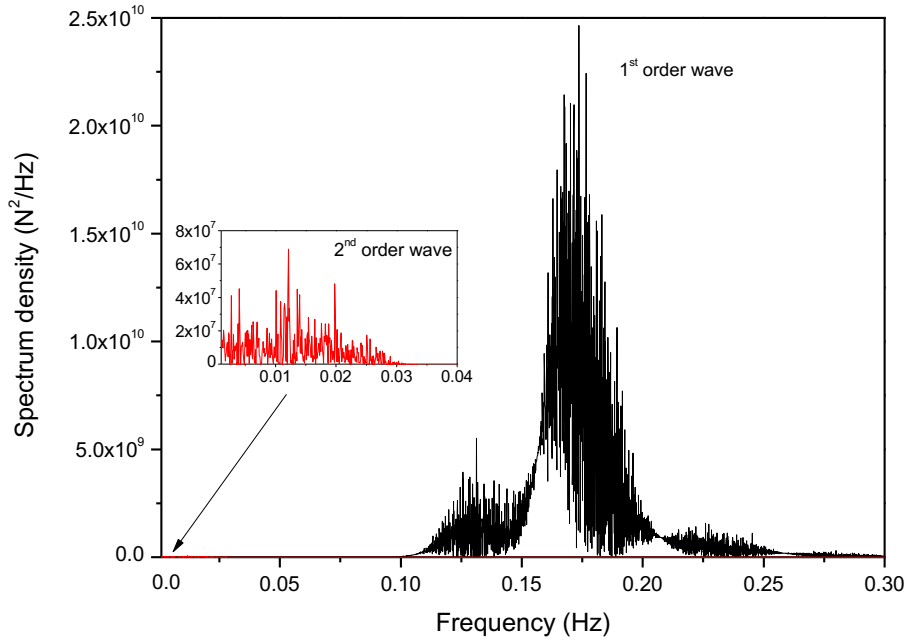Figure 6. Typical first-order and second-order wave force time histories in the x-direction.

Figure 7. Spectrum densities of the first-order and second-order wave loads.

4. Wind load

The instantaneous wind speed can be split into a mean wind part and a fluctuating wind part as shown in Figure 8. The total wind speed $U_{total}(z,t)$ can be calculated by:

$$U_{total}(z,t)=U_{m}(z)+u(z,t),\qquad(10)$$

where $U_{m}(z)$ and $u(z,t)$ represent the mean and the fluctuating wind component, respectively. z is the height above the sea surface.
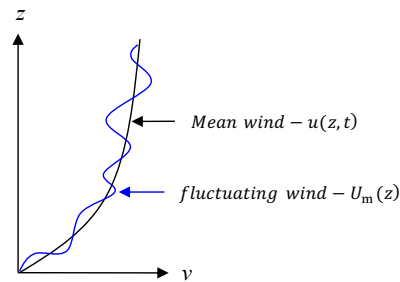

Figure 8. A typical wind speed profile.

4.1 Mean wind component

The mean wind part is a constant wind velocity for each height during a stationary period which is usually taken as 10 minutes (Jia 2014). The wind speed distributes over the height z by the power law relationship

$$U_{\mathrm{m}}(z) = U_{\mathrm{ref}}(\frac{z}{z_{\mathrm{ref}}})^{\alpha},\tag{11}$$

where U_{ref} is the wind speed at the reference height z_{ref}, α is the power coefficient counting for the shape effect. Like the wave data, no measurements of the wind climate have been available when this study was conducted. In this study, the reference height is selected at 10 m above the sea surface and the wind speed at 10 m reference height is 31.7 m/s^2 (COWI 2016). Further investigations related to the wind climate will be performed when the results from wind measurements are available.

4.2 Turbulent wind component

The fluctuating part of the wind speed is simulated by considering the wind spectra and the coherence function to maintain the spatial statistical properties. The wind spectrum at any point in the wind field is calculated by the following equation (Aas-Jakobsen 2015),

$$S_{ii} = \frac{I_i^2 U_{10\mathrm{min}} L_i}{\left(1 + 1.5 \cdot \dfrac{f \cdot L_i}{U_{10\mathrm{min}}}\right)^{5/3}}\tag{12}$$

where S_{ii} is the spectrum in any direction at any point. I_i is the turbulence intensity and $U_{10\mathrm{min}}$ is the 10-minutes mean wind speed. L_i is the length scale in any direction and f is the wind frequency.

The simultaneity of wind gusts at different locations and frequencies is represented by the coherence spectrum. In this study, the coherence between any two locations is calculated by means of Equation 13

$$\sqrt{\mathrm{coh}(f,s)} = \exp(-\frac{c_i \cdot f \cdot s}{U_{10\min}}), \qquad (13)$$

where c_i is the decay exponent and s is the separation distance between any two locations.

4.3 Wind load application

The dynamic wind load is based on a wind field established by means of the program WindSim (Aas-Jakobsen 2015). The wind field is then converted into three force components for each element: lift, drag and moment where the lift force and the drag force are perpendicular and parallel to the wind direction, respectively. The moment rotates around the axial axis of the elements. The interaction between the wind and the structure are defined by the force coefficients. For example, the drag force component can be calculated by

$$F_d = \frac{1}{2} \cdot \rho \cdot C_D \cdot \upsilon_r \cdot |\upsilon_r| \cdot d, \qquad (14)$$

where F_d is the drag force and C_D is the drag coefficient. υ_r is the relative velocity of the structure and wind field and d is the diameter of the component. Both the lift coefficient C_L and moment coefficient C_M are defined in a similar manner.

For the twin-girder bridge model, the resulting drag force is affected by the gap between these girders (Chen et al. 2014).The effect is accounted for by assuming that the windward box girder will experience a larger resulting drag force than the leeward one. In this study, an equivalent drag coefficient is taken as the mean value of the two

drag force coefficients for the leeward and windward girders (Larsen 1998). For the other structural parts, the drag coefficients are chosen according to Eurocode 1 (En 1991). The lift and moment coefficients are selected based on the work from A. Larsen (Larsen 1998). The coefficients for different cross sections are presented in Table 3. Due to software limitation in the number of nodes, the wind field coherence is only calculated in the middle part of the bridge. Outside of this area, the wind velocity is assumed to be fully correlated with the nearest nodes in the grid.

Table 3. Aero dynamical coefficients for bridge components.

Bridge component	Item	Value
Girder	C_D	0.55
	C_L	0.122
	C_M	0.051
Tower	C_D	0.8
Cable	C_D	0.84
Column	C_D	0.77

5. Time domain simulation of the bridge response

With the above wave and wind inputs ready, time domain simulations are conducted to investigate the bridge response under various loading conditions. Four load combinations are simulated: (1) first-order wave load only, (2) first-order and second-order wave loads, (3) wind load only, and (4) all wave and wind loads. All wave loads are assumed to have zero heading to the pontoons and the wind load comes from the same direction (west to east) as shown in Figure 9. It should be noted that only the response of the west girders and west cables are discussed in the following section. The response of the parallel east girders is similar.

5.1 Typical girder and cable responses

The bridge response at two typical locations in the bridge girder is investigated herein.

As shown in Figure 9, Node 1 is located at the cable-stayed span while Node 2 is at the continuous span in the mid-bridge. The first west cable from the right as shown in Figure 9 is selected to investigate the axial force for different excitation loads.
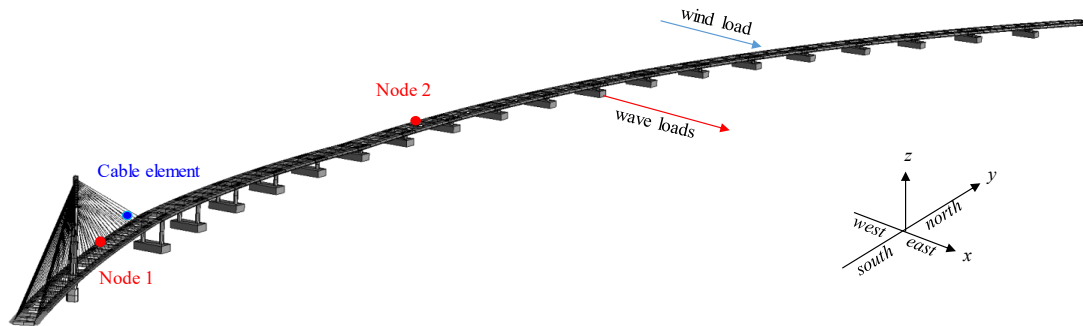

Figure 9. The direction of external excitation loads and the selected nodes and cable element.

First, the transverse displacement time histories of Node 1 are compared in Figure 10 (a). It is observed that both the wind and wave loads contribute to the transverse motion of the bridge girder. However, the wind load results in a much larger response than the wave load. The transverse displacement has a mean value of around 0.3 m due to the mean wind component. The wave load induced transverse motion has its mean at 0 m and the maximum displacement is about 0.3 m. The displacement contributions from different wave and wind loads are also evident from the frequency plot in Figure 10 (b).

Figure 11 shows the transverse response of Node 2 at the continuous span for various loading conditions. The wave-induced displacement is in the same range as Node 1 in the cable-stayed span. However, the wind load results in a significantly larger transverse motion with a maximum displacement of 2 m. A similar observation can be found in the frequency domain plot in Figure 11 (b). Again, the wind load has much larger amplitude and thus dominates the bridge transverse motion in the continuous

spans. A contribution of the second-order wave load can also be clearly observed in the continuous spans.
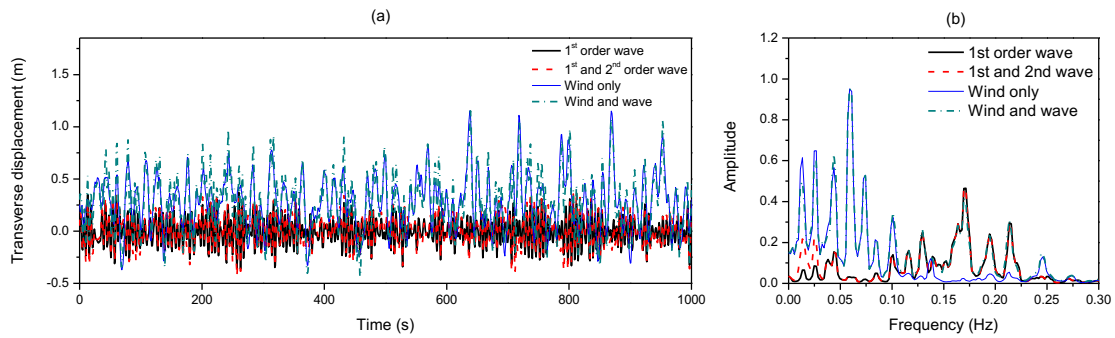

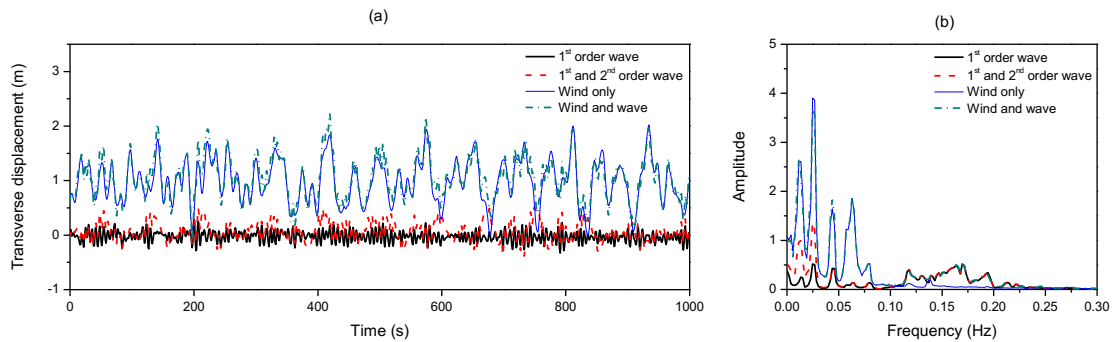Figure 10. (a) Time history and (b) frequency domain plots of the transverse displacement for Node 1.

Figure 11. (a) Time history and (b) frequency domain plots of the transverse displacement for Node 2.

The displacement time histories in the vertical direction, for Node 1 in the cable-stayed span are shown in Figure 12 (a). The contributions from different excitation loads in the vertical direction are similar to that in the transverse direction. The frequency plot in Figure 12 (b) is generally similar to the transverse frequency plot in Fig 10 (b). However, a second peak of the wind-induced response can be found at a higher frequency. This suggests the wind load may excite some higher vertical vibration modes of the bridge in the cable-stayed spans.

Figure 13 (a) shows the vertical response of Node 2 at the continuous span. The wind load still dominates the vertical motion. However, the influence is less significant compared to that in the transverse direction. This can also be observed by comparing the

amplitudes in the frequency plots in Figure 13 (b) and Figure 11 (b). The contribution from the first-order wave load is relatively small and the second-order wave load has almost no effect on the bridge vertical motion.
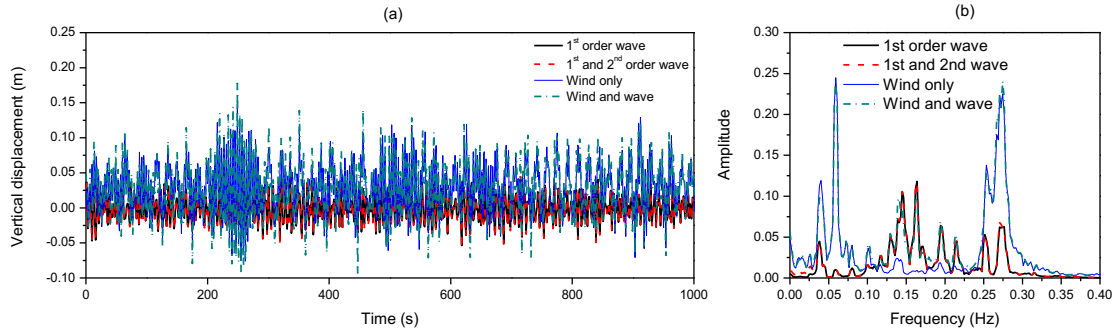

Figure 12. (a) Time history and (b) frequency domain plots of the vertical displacement for Node 1.
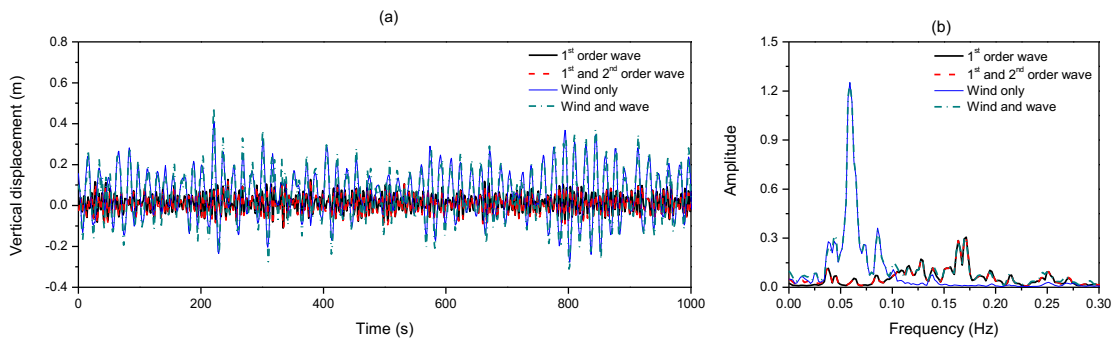

Figure 13. (a) Time history and (b) frequency domain plots of the vertical displacement for Node 2.

The axial force time histories and frequency plots of the selected cable element are illustrated in Figure 14 (a) and 14 (b), respectively. It can be clearly observed that the wind load has the greatest influence in the cable axial force while the second-order wave load has almost no effect. This trend is in line with the girder motion in the cable-stayed span. The maximum axial force is around 6 MN. With a cross-sectional area of around 0.0138 m^2, this force level only corresponds to an axial stress of 434 MPa. The stress level corresponds to a utilization level of 23.4% which is much lower than the acceptable utilization ration of 56%.
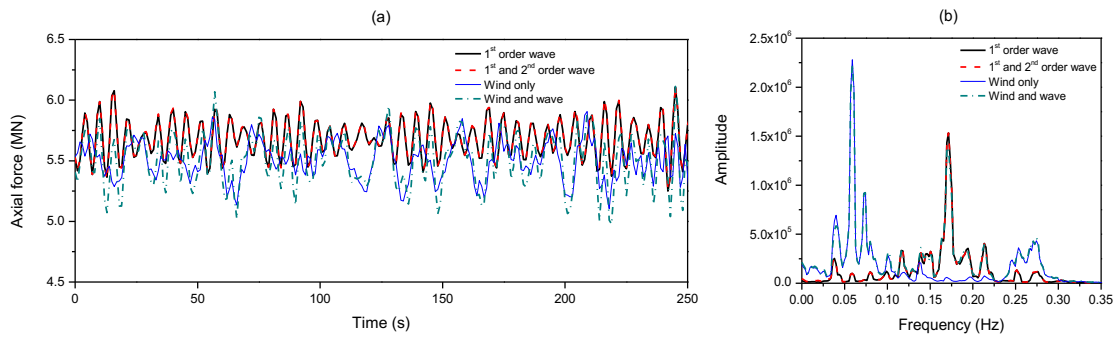
Figure 14. (a) Time history and (b) frequency domain plots of the cable axial force.

5.2 Bridge motions along the bridge girders

Based on the above analysis, typical transverse and vertical motions of the bridge girder at the cable-stayed span and the continuous span are obtained. Further, it is interesting to investigate how the whole bridge behaves under various loading conditions.

The maximum transverse displacements along the bridge girder for different load combinations are shown in Figure 15 (a). The contributions from the first-order and second-order wave loads are in a similar range. The maximum transverse displacement under the action of the total wave load is about 0.6 m in the middle of the bridge. The wind load has a significant effect on the transverse motion of the bridge. The maximum displacement is about 2.6 m which is much larger than the response induced by the wave loads. The bridge displacement under combined wind and wave loadings is close to the case with wind load only. It is interesting to note that the displacement under the wind load is not symmetric about the bridge centre. This may be attributed to the different structural geometries at the two sides. The cable-stayed part in the south has relatively smaller transverse stiffness than the continuous part in the north. In addition, the girder clearance in the cable-stayed span (55 m) is higher than in the continuous span (11.75 m). The girder will, therefore, be exposed to larger wind velocities and undergo larger transverse displacements.

The vertical displacements of the bridge girder are plotted in Figure 15 (b). As expected, the second-order wave load has almost no contribution to the vertical motion of the bridge. The vertical displacement of the bridge girder under the first-order wave load has a maximum value of 0.25 m. The contribution from the wind load is in a similar range as that from the wave load. The maximum vertical displacement under the total environmental load is about 0.5 m.

One of the important considerations in the design of bridges is the maximum vertical acceleration of the bridge deck. It is required that the vertical acceleration should not exceed some 0.6 m/s^2 (Seif and Inoue 1998) to allow safe traffic and the comfortableness of the bridge users. As shown in Figure 15 (c), the maximum vertical acceleration in the continuous part is less than 0.4 m/s^2 in all cases. For the cable-stayed part in the south, the wind-induced vertical acceleration is close to the limit of 0.6 m/s^2, which is considerably larger than that in the continuous spans in the north. This is because the cable-stayed span is more than twice the length of the continuous span.

Therefore, special design considerations should be exercised to limit the vertical vibration of the cable-stayed spans. Passive linear and nonlinear dampers have been widely used to suppress vibration of the stay cables (Main and Jones 2001). Tuned mass dampers (TMD) and shape memory alloys dampers (SMA) are the most commonly used damper systems (Cai et al. 2007, Dong et al. 2010). These devices can effectively reduce cable vibrations. It is found that the cable vibration can be reduced to about 20% of that without the damping devices (Cai, Wu and Araujo 2007).
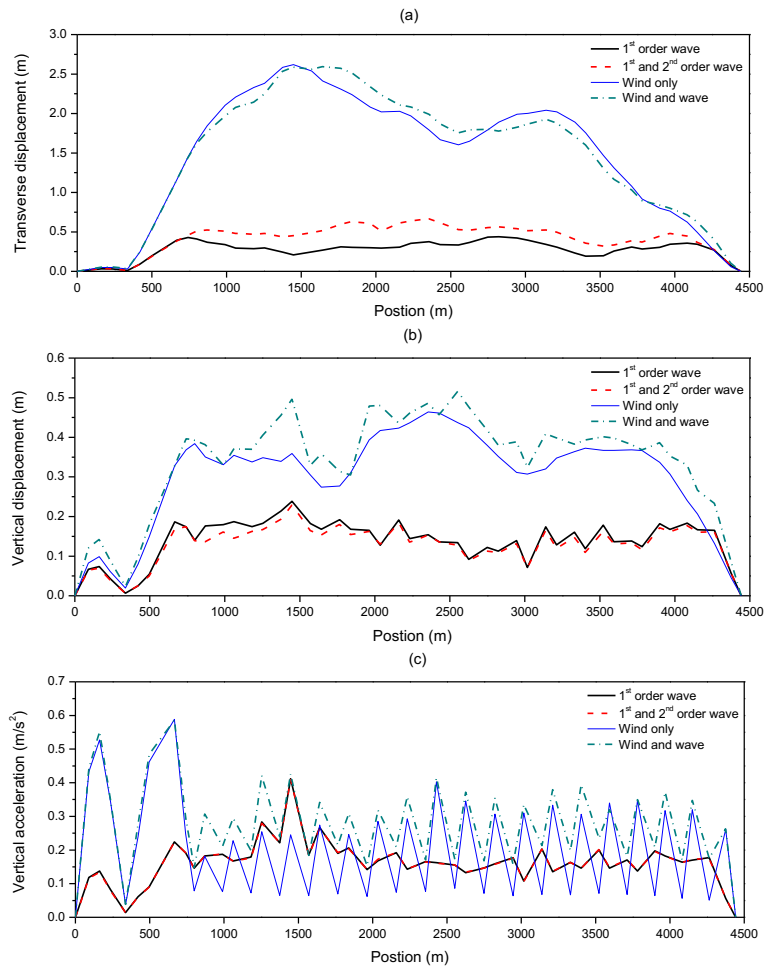
Figure 15. (a) Transverse displacement, (b) vertical displacement, and (c) vertical acceleration of the girder along the bridge.

5.3 Bending and torsional moments along the bridge girders

The bending moment of the bridge girder about the strong axis (z) is plotted in Figure 16 (a). In the cable-stayed spans, the strong axis moment due to the wind load is much larger than that induced by the wave loads. In the continuous spans, however, the first-order wave load results in a larger strong axis moment than that induced by the wind load. This observation matches the transverse displacement distribution in Figure 15 (a). The displacement increases dramatically from 500 m to 1000 m while it has a much smaller variation in the middle part of the bridge.

Figure 16 (b) shows the weak axis moment along the bridge girder. The first-order wave load controls the weak axis bending moment and the second-order wave

load has almost no effect. It is interesting to find that although the wind load results in a similar magnitude of the vertical motion as the first-order wave load, it has little effect on the girder weak axis moment. This is because the wind load induced vertical motion is generally in phase at each pontoon and thus results in a smaller weak axis moment.

The torsional response of the bridge girder is shown in Figure 16 (c). The wind load dominates the torsional moment in the cable-stayed spans while the first-order wave load has the most significant effect on the torsional response in the continuous spans. The wind load also contributes to the torsional moment of the middle part of the bridge. The second-order wave load has almost no effect on the bridge torsional response.
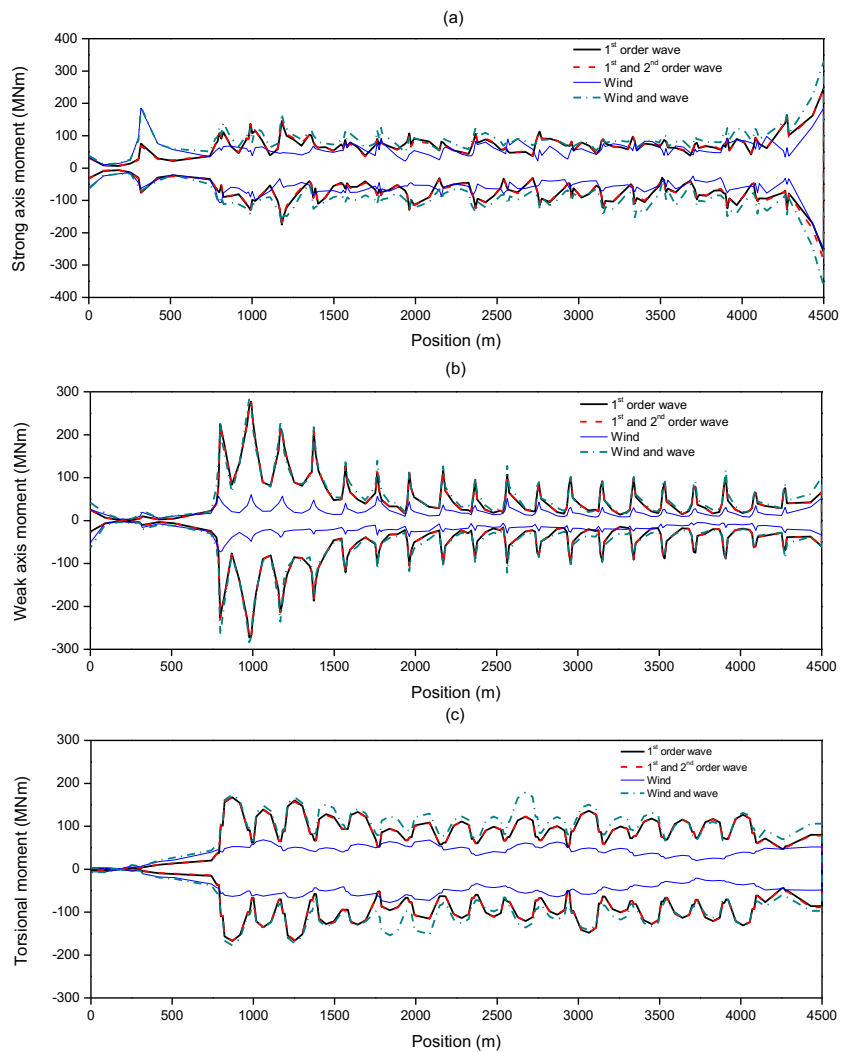
Figure 16. (a) Strong axis, (b) weak axis and (c) torsional moment of the girder along the bridge.

5.4 Discussion

The response of the floating bridge responses to various wind and wave load conditions have been simulated and compared.

The wind load has a large contribution to the bridge motion. It dominates both the transverse and vertical motions of the bridge girder. The mean wind component induces a large transverse displacement of more than 2 m. The girder deformation shape in Figure 15 (a) is similar to the first mode of bridge vibration as shown in Fig 4. This suggests that the low-frequency wind load may excite some of the horizontal bending modes of the bridge. The vertical acceleration in the cable-stayed span is large due to the wind loading. The wind load induces higher bending and torsional moments in the cable-stayed spans than in the continuous spans.

The first-order wave load contributes also to the bridge motion in the transverse and vertical directions. The effect is smaller than the wind load as can be observed from the displacement time histories and frequency plots. However, the first-order wave load results in larger moments in the bridge girder in all three rotational degrees of freedom.

The second-order wave load influences the transverse motion of the bridge girders, especially in the continuous spans. However, it has a negligible effect on the vertical motions of the bridge.

Based on the above discussions, the following recommendations can be given to improve the current design. In the cable-stayed spans, a vibration-control damper system as discussed in Section 5.2 may be installed to limit the vertical motion of the bridge girder and thus ensure a safe traffic. As shown in Figure 16 (c), large weak axis moments due to the pendulum mode of the pontoons are observed in the cable-stayed

spans. This can be improved by strengthening the girders locally or introducing an additional connection between the pontoons in axis 3 and 4. For the whole bridge, high reaction moments occur in the girders at the connection to the supporting column. Therefore, the girder sections at these locations should also be strengthened locally.

There are several issues which may be of interests for further investigations.

1. No global buckling was observed under the environmental loads in this study. However, there may be a potential issue regarding the buckling of the bridge in extreme environmental conditions. Further studies should be conducted to evaluate the global buckling of the bridge. The accidental limit state design including ship collision loads should also be carefully checked (Sha and Amdahl 2017).

2. The bridge model is established with beam elements only, it is sufficient to identify the critical structural members of large plastic utilization. The local behaviour, plate buckling, for instance, is neglected in the analysis. However, this analysis can be used as the basis for additional local checks with detailed shell elements at the critical locations.

3. For the wind and wave data, no measurements have been available when the current analysis is conducted (COWI 2016). Further investigations should be conducted when the results from site measurements are available. The analysis in this study only considers the wind and wave loadings from the west to the east, i.e. zero incidence angle. A further study can be conducted to investigate environmental loads with different headings. Bridge responses from short-crested waves can also be of interest in the future study.

6. Conclusions

In this study, a numerical model of a floating bridge is established. Dynamic time domain analysis is conducted to investigate the bridge response under environmental

loadings. The first-order and second-order wave loads are calculated by using the transfer functions obtained from a WADAM analysis based on the linear potential theory. The dynamic wind load is also included numerically by generating a wind velocity field in WindSim and applied to the structural model. The bridge responses under various wind and wave load combinations are investigated.

It is found that the wind load dominates the girder transverse displacement and it has a large effect on the vertical displacement of the bridge girder. The axial force of the cable is controlled by the wind load. The axial force level is moderate and well below utilization limits. The wind-induced vertical acceleration in the cable-stayed spans is close to the safety limit and a vibration reduction system should be designed and installed.

Compared with the wind load induced motion, the first-order wave load has a small effect on the bridge motion in the transverse direction and a comparable contribution in the vertical direction. The second-order wave load only has a limited contribution to the transverse bridge displacement.

The first-order wave load has a dominant influence on all bending and torsional moments of the bridge girder while the second-order wave load has almost no contribution to the girder response. The wind load induces large bending and torsional moments in the cable-stayed spans. In addition, it also contributes to the torsional moment of the girders in the middle bridge.

Acknowledgements

References

Aas-Jakobsen K. 2015. User manual WindSim.

Aas-Jakobsen K, Strømmen E. 1998. Time domain calculations of buffeting response for wind-sensitive structures. Journal of Wind Engineering and Industrial Aerodynamics.74:687-695.

Boonyapinyo V, Yamada H, Miyata T. 1994. Wind-induced nonlinear lateral-torsional buckling of cable-stayed bridges. Journal of Structural Engineering.120:486-506.

Cai C, Wu W, Araujo M. 2007. Cable vibration control with a TMD-MR damper system: Experimental exploration. Journal of structural engineering.133:629-637.

Cao Y, Xiang H, Zhou Y. 2000. Simulation of stochastic wind velocity field on long-span bridges. Journal of Engineering Mechanics.126:1-6.

Chakrabarti SK. 1987. Hydrodynamics of offshore structures: WIT press.

Chen W-L, Li H, Hu H. 2014. An experimental study on the unsteady vortices and turbulent flow structures around twin-box-girder bridge deck models with different gap ratios. Journal of Wind Engineering and Industrial Aerodynamics.132:27-36.

COWI. 2016. NOT-KTEKA-021 Curved bridge - Navigation channel in south. Oslo, Norway.

Dong J, Cai C, Okeil AM. 2010. Overview of potential and existing applications of shape memory alloys in bridges. Journal of Bridge Engineering.16:305-315.

En B. 1991. 1-4: 2005 Eurocode 1: Actions on structures—General actions—Wind actions. In: NA to BS EN.

Faltinsen O. 1993. Sea loads on ships and offshore structures: Cambridge university press.

Hasselmann K, Barnett T, Bouws E, Carlson H, Cartwright D, Enke K, Ewing J, Gienapp H, Hasselmann D, Kruseman P. 1973. Measurements of wind-wave growth and swell decay during the Joint North Sea Wave Project (JONSWAP).

Hilber HM, Hughes TJ, Taylor RL. 1977. Improved numerical dissipation for time integration algorithms in structural dynamics. Earthquake Engineering & Structural Dynamics.5:283-292.

Institution BS. 2004. Eurocode 2: Design of Concrete Structures: Part 1-1: General Rules and Rules for Buildings. In: British Standards Institution.

Jia J. 2014. Investigations of a practical wind-induced fatigue calculation based on nonlinear time domain dynamic analysis and a full wind-directional scatter diagram. Ships and Offshore Structures.9:272-296.

Kvittem MI, Bachynski EE, Moan T. 2012. Effects of hydrodynamic modelling in fully coupled simulations of a semi-submersible wind turbine. Energy Procedia.24:351-362.

Larsen A. 1998. Advances in aeroelastic analyses of suspension and cable-stayed bridges. Journal of Wind Engineering and Industrial Aerodynamics.74:73-90.

Livesley RK. 2013. Matrix Methods of Structural Analysis: Elsevier.

Main J, Jones N. 2001. Evaluation of viscous dampers for stay-cable vibration mitigation. Journal of Bridge Engineering.6:385-397.

Newman JN. Second-order, slowly-varying forces on vessels in irregular waves. Proceedings of the Proc Int Symp Dyn Mar Vehic Struct in Waves, Inst Mech Engrs, London, 1974; 1974.

Salvatori L, Borri C. 2007. Frequency-and time-domain methods for the numerical modeling of full-bridge aeroelasticity. Computers & structures.85:675-687.

Santos J, Miyata T, Yamada H. Gust response of a long span bridge by the time domain approach. Proceedings of the Proceedings of Third Asia-Pacific Symposium on Wind Engineering, Hong Kong; 1993.

Seif MS, Inoue Y. 1998. Dynamic analysis of floating bridges. Marine structures.11:29-46.

Sha Y, Amdahl J. Ship Collision Analysis of a Floating Bridge in Ferry-Free E39 Project. Proceedings of the ASME 2017 36th International Conference on Ocean, Offshore and Arctic Engineering; 2017: American Society of Mechanical Engineers.

Søreide TH, Amdahl J, Eberg E, Holmås T, Hellan Ø. 1993. USFOS-A computer program for progressive collapse analysis of steel offshore structures. Theory Manual. SINTEF STF71 F88038 Rev.

Veritas DN. 1994. WADAM—Wave Analysis by Diffraction and Morison Theory, SESAM user's manual, Høvik.

Watanabe E, Utsunomiya T, Wang C. 2004. Hydroelastic analysis of pontoon-type VLFS: a literature survey. Engineering structures.26:245-256.